

# Probabilistic Prognosis of Non-Planar Fatigue Crack Growth

Patrick E. Leser<sup>1</sup>, John A. Newman<sup>1</sup>, James E. Warner<sup>1</sup>, William P. Leser<sup>1</sup>, Jacob D. Hochhalter<sup>1</sup>, and Fuh-Gwo Yuan<sup>2</sup>

<sup>1</sup> *NASA Langley Research Center, Hampton, VA, 23681, USA*  
*patrick.e.leser@nasa.gov*

<sup>2</sup> *North Carolina State University, Raleigh, NC, 27695, USA*

## ABSTRACT

Quantifying the uncertainty in model parameters for the purpose of damage prognosis can be accomplished utilizing Bayesian inference and damage diagnosis techniques such as non-destructive evaluation or structural health monitoring. The number of samples required to solve the Bayesian inverse problem through common sampling techniques (e.g., Markov chain Monte Carlo) renders high-fidelity finite element-based damage growth models unusable due to prohibitive computation times. However, these types of models are often the only option when attempting to model complex damage growth in real-world structures. Here, a recently developed high-fidelity fatigue crack growth model is used which, when compared to finite element-based modeling, has demonstrated reductions in computation times of three orders of magnitude through the use of surrogate models and machine learning. A probabilistic prognosis framework incorporating this model is developed and demonstrated for non-planar crack growth in a modified edge-notched aluminum tensile specimen. Predictions of remaining useful life are made over time for five updates of the damage diagnosis data, and prognostic metrics are utilized to evaluate the performance of the prognostic framework. Challenges specific to the probabilistic prognosis of non-planar fatigue crack growth are highlighted and discussed in the context of the experimental results.

## 1. INTRODUCTION

Probabilistic damage prognosis is an essential aspect of any aerospace structural health management system. The ability to predict how damage will propagate in a structure with confidence and in the face of uncertainties can be an invaluable tool to operators making mission- or safety-critical de-

isions. The applications of probabilistic damage prognosis are widespread, including but not limited to concepts such as condition-based maintenance (Farrar & Worden, 2012) and long endurance missions (e.g., unmanned aircraft systems or spacecraft) for which maintenance is not an option. The degree of fidelity in the models used to make these forecasts can vary from simple approximations to high-fidelity finite element models with millions of degrees of freedom.

There has been extensive research in the area of coupling SHM and NDE with damage prognosis, a few notable examples of which are as follows. Liu and Mahadevan proposed a new way to quantify the uncertainty in equivalent initial flaw sizes, which they used in conjunction with an analytical fatigue crack growth model to produce probabilistic predictions of fatigue life in metallic specimens (Liu & Mahadevan, 2009). Gobbato et al. combined NDE with probabilistic models of both damage evolution and future aerodynamic loading through Bayesian inference (Gobbato, Conte, Kosmatka, & Farrar, 2012). Peng et al. demonstrated a direct link between Lamb wave-based damage detection and probabilistic prognosis for a metallic lap joint using analytical crack growth laws and Bayesian inference (Peng, He, et al., 2015). In recent years, researchers have also investigated fatigue damage prognosis for composite materials, joining Lamb wave-based diagnosis with analytical stiffness degradation models through Bayesian approaches (Chiachio, Chiachio, Saxena, Rus, & Goebel, 2013; Peng, Liu, Saxena, & Goebel, 2015). Note that all of these works are probabilistic. Without probability, it is often impossible to make predictions with confidence. Without confidence, the risk in making mission- or safety-critical decisions becomes unacceptable.

Much of the research conducted and discussed thus far would be considered low-fidelity approaches. However, application to damage in real-world structures is key to unlocking the potential of damage prognosis. High-fidelity FE models are

---

Patrick Leser et al. This is an open-access article distributed under the terms of the Creative Commons Attribution 3.0 United States License, which permits unrestricted use, distribution, and reproduction in any medium, provided the original author and source are credited.

now capable of modeling the complexities of real-world damage, but these models are often prohibitively time-intensive. This limitation is the primary reason these models are seldom used in probabilistic prognosis and do not appear in the aforementioned research efforts. Many of these works rely on Bayesian inference and sampling techniques such as Markov chain Monte Carlo (MCMC) to develop probabilistic life predictions. MCMC can require anywhere from thousands to millions of simulations to provide meaningful results (Smith, 2013). FE-based simulations which conservatively take on the order of a few hours to complete could result in total prediction times on the order of years. While efforts are being made to parallelize these statistical techniques (Ter Braak, 2006; Vrugt et al., 2009; Laloy & Vrugt, 2012; Neiswanger, Wang, & Xing, 2014), parallelization is, in general, not a feasible option at this time due to the serial nature of MCMC techniques.

Some researchers have taken strides to bridge the gap between probabilistic prognosis and high-fidelity modeling, primarily through the use of machine learning. In general, the time consuming aspects of high-fidelity damage growth simulations can be replaced by a surrogate model, trained via supervised machine learning, which can quantitatively represent the primary features of the high-fidelity model being replaced but at a decreased computational cost. Sankararaman et al. trained surrogate models to replace expensive finite element solutions of crack driving forces for a cylindrical specimen subjected to multi-axial loading using a characteristic plane approach (Sankararaman, Ling, Shantz, & Mahadevan, 2011; Sankararaman, Ling, & Mahadevan, 2011). Expanding upon this work, Ling and Mahadevan coupled the surrogate model-based, characteristic plane approach with damage diagnosis data to forecast fatigue damage growth in aluminum specimens with quantified uncertainties (Ling & Mahadevan, 2012). As a natural extension, Hombal et al. developed a two-stage planar approximation for non-planar crack growth (Hombal, Ling, Wolfe, & Mahadevan, 2012). A more advanced surrogate modeling methodology was proposed by Hombal and Mahadevan to predict three-dimensional damage growth under multi-axial, time varying fatigue loading (Hombal & Mahadevan, 2013). The complex crack growth was simulated in a reduced-order space, allowing for supervised learning without the need for planar approximations. The resultant crack growth simulations benefited from a significant reduction in computation times.

The aforementioned research into rapid, high-fidelity damage prognosis is promising; however, there remains a dearth of flexibility in these proposed models. For example, the three-dimensional surrogate modeling approach presented in

(Hombal & Mahadevan, 2013) is arguably the most sophisticated technique discussed above since it does not require any planar assumptions. However, since the crack growth steps are internal to the surrogate model, the crack growth parameters are fixed unless accounted for in the initial training matrix. At best, this prevents the use of model selection algorithms to determine an ideal crack growth law. At worst, this means that uncertainty in crack growth rate parameters cannot be accounted for in a prognostic framework. The latter issue is detrimental, as a large portion of the uncertainty in remaining useful life (RUL) predictions for fatigue-driven damage results from scatter in the crack growth rate parameters (Johnston, 1983; Gope, 1999). While surrogate modeling is an excellent approach for reducing computation times of high-fidelity models, care must be taken not to restrict the dimensionality of the parameter space considered in the Bayesian inverse problem. This is especially important since supervised learning with high-dimensional input spaces can cause both a decrease in predictive accuracy and an increase in storage requirements.

Recently, (Leser et al., 2016) proposed an alternative approach to reducing computation times associated with high-fidelity damage growth modeling. To address the issue of flexibility, the surrogate model is confined to only a sub-component of the overall damage growth model. Particularly, the surrogate model replaces the high-fidelity, FE-based computation of the damage driving forces; e.g., stress-intensity factors (SIF) or energy release rates. It was determined that the solution of the finite element system of equations was the primary driver of the exorbitant computation times. By restricting the surrogate model to this portion of the modeling process, model parameters such as those associated with the crack growth rate were not dependent on the machine learning process. As a result, both high degrees of fidelity and flexibility were achieved while simultaneously reducing computation times by over three orders of magnitude. The present paper expands on this work by providing a more rigorous demonstration of the predictive capabilities offered by the surrogate modeling approach in the context of non-planar crack growth. In particular, the effects of noise in two dimensions is discussed along with an example of model discrepancy and how it poses dangers in the context of probabilistic prognosis.

## 2. PROGNOSIS FRAMEWORK

The prognosis framework is composed of the following four components: (i) parameter estimation and uncertainty quantification through Bayesian inference, (ii) global sensitivity analysis to determine the parameters that contribute the most

variance to the final prediction, (iii) the crack growth model, and (iv) the prognostic metrics used to quantitatively assess the performance of the framework. The first two components are common to probabilistic prognosis; thus, discussions of these topics will be limited for brevity. In contrast, the third and fourth components are potentially unfamiliar to the reader and will be discussed in enough detail to promote understanding of the results.

### 2.1. Uncertainty Quantification and Propagation

The methods used here are based on the incorporation of SHM or NDE with a given damage model in order to make a prediction of remaining useful life for a unique component or structure. This can be accomplished by making discrete observations of the damage state throughout the life of the monitored component, combining this information with prior knowledge (e.g., knowledge of the component geometry, applied loads, and the material), and inversely quantifying the uncertainties in the damage model through Bayesian inference. This uncertainty can then be propagated back through the model, allowing for extrapolation to future time instances. Bayes Theorem also provides flexibility in how these predictions are updated as more observations are made.

The relationship between a parameter-dependent model response,  $f_k(Q)$ , measurement errors,  $\varepsilon_k$ , and experimental measurements,  $\Upsilon_k$ , is given by the statistical model

$$\Upsilon_k = f_k(Q) + \varepsilon_k, \quad (1)$$

where  $f_k(Q)$ ,  $\varepsilon_k$ , and  $\Upsilon_k$  are random variables and the measurement errors are assumed to be unbiased, independent and identically distributed. Here,  $Q$ , also a random variable, denotes the model parameters, and has realizations  $q$ . The index of the available observations,  $k = 1, \dots, n_{obs}$  where  $n_{obs}$  is the total number of observations. The solution to the Bayesian inverse problem is the posterior density,  $\pi(q|v_{obs})$ , which is the best estimate of the parameter densities based on experimental observations and prior knowledge of the parameter distributions,  $\pi_0(q)$ . Formally, the relationship between the posterior density, the prior density, and the observations is given by Bayes' Theorem, which takes the form

$$\pi(q|v_{obs}) = \frac{\pi(v_{obs}|q)\pi_0(q)}{\pi(v_{obs})} = \frac{\pi(v_{obs}|q)\pi_0(q)}{\int_{\mathbb{R}^p} \pi(v_{obs}|q)\pi_0(q)dq} \quad (2)$$

where  $p$  is the number of parameters and defines the dimension of the integral in Equation 2. Assuming normally dis-

tributed errors,  $\varepsilon_k \sim N(0, \sigma^2)$ , damage diagnosis data are incorporated through the likelihood,

$$\pi(v_{obs}|q) = \frac{1}{(2\pi\sigma^2)^{n_{obs}/2}} \exp\left(-\sum_{k=1}^{n_{obs}} [v_{obs,k} - f_k(q)]^2 / 2\sigma^2\right), \quad (3)$$

Equation 2 can be solved directly for simple problems of low dimensionality, but, for most practical models, the direct solution to the inverse problem becomes intractable. Quadrature and sparse grid techniques can be used in certain cases with low dimension; i.e.,  $p \leq 6$  (Smith, 2013). An alternative approach is to use Markov chain Monte Carlo (MCMC) techniques. Utilizing assumed attributes of the posterior density, such as those used to define Equation 3, Markov chains can be constructed for the model parameters based on the observed measurements. The stationary distributions of the chains constructed in this manner is the sought-after posterior density, thus approximating a solution to the inverse problem.

### 2.2. Global Sensitivity Analysis

Variance-based global sensitivity analysis can be conducted to determine the contribution of parameter uncertainty to the output uncertainty (Saltelli et al., 2008; Smith, 2013). By analyzing parameter sensitivity, non-influential parameters can be identified; i.e., the parameter,  $Q_i$  for  $i = 1, \dots, p$  where the influence,  $\mathcal{I}(Q_i) \approx 0$ . These are parameters that do not have a significant effect on the output uncertainty. As such, these parameters can be removed from the Bayesian inference procedure. This is critical because the number of samples required to reliably represent the posterior distribution is directly dependent on the number of parameters,  $p$ , i.e., the dimension of the multivariate distribution. Fewer samples means a faster solution to the inverse problem. Herein, the Saltelli algorithm (Saltelli et al., 2008) was implemented to compute both the first order and total-effect Sobol' indices. It should be noted that this method relies on the assumption that all of the parameters are independent (i.e., uncorrelated).

### 2.3. Fatigue Crack Growth Model

The most expensive aspect of high-fidelity, FE-based fracture modeling is the solution of the finite element equations. The remeshing at each growth step is relatively fast. The mesh-independent tracking of the crack geometry in three-dimensional space is even faster, which is the basis for the model developed in (Leser et al., 2016) and used in the present work. The fatigue crack growth model is essentially a three dimensional fracture mechanics algorithm wrapped

around a set of externally trained surrogate models which replace the finite element analysis (FEA) component of high-fidelity fracture modeling. The code tracks a given crack front in space and evolves the crack based on driving forces obtained from the surrogate models. The code was developed using the Python computing language (Van Rossum & Drake, 2011) as a general tool to reduce computation times associated with high-fidelity fracture simulation and is not limited to the work presented herein.

A diagram illustrating the geometrical and symbolic basis of the model is shown in Figure 1. The user defines the geometry of the part or component in which the crack resides, the initial crack front, and any required model parameters (e.g., Paris' Law parameters). A component geometry is established as a set of points,  $G \subset \mathbb{R}^3$ , a crack is initialized within this component, and the crack is grown step-by-step by either a finite number of cycles per step or a median crack front extension. For any time,  $t$ , the crack front,  $\Gamma(t)$ , exists in Cartesian space as a  $3 \times \Omega$  array, where  $\Omega$  is the total number of explicitly defined crack front points,  $\gamma_\omega$ . Each crack front point for  $\omega = 1, \dots, \Omega$  is a point in the Cartesian frame. In this sense,  $\gamma_\omega \in \Gamma \subset G$  at any time,  $t$ . For each growth step, crack driving forces at each point are returned from the surrogate models based on the boundary conditions applied to the component and the current geometrical state of the crack front. These driving forces dictate how the crack evolves. At each growth step, any crack front points that have grown outside of the geometry (i.e.,  $\gamma_\omega \notin G$ ) are deleted, and a new crack front  $\Gamma$  is derived using a polynomial or spline fit. The curve is extrapolated to the points at which it intersects with the component or part geometry boundaries, and then  $\Omega$  evenly spaced points are interpolated between (and including) these end points. The time varying crack path can be tracked by storing the  $\Gamma(t)$  instance at each growth step. This process is iterated until a stopping condition is reached.

FEA-based methods traditionally compute the crack driving forces at each growth step by either an explicit representation where the crack surface and component assembly is remeshed at each step, or through the use of enriched elements (e.g., XFEM). In either case, the system is solved and the displacements are used to compute the crack driving forces. As discussed, the finite element solution is typically the most computationally intensive part of this process. Therefore, the proposed crack growth model replaces this process with a surrogate modeling approach. Here, a large number,  $\Phi$ , of crack growth simulations are run using a FE-based, high-fidelity fracture mechanics code *a priori*, or without knowledge of the true crack path. Each of these simulations are then broken down by growth step, meaning that each explicitly mod-

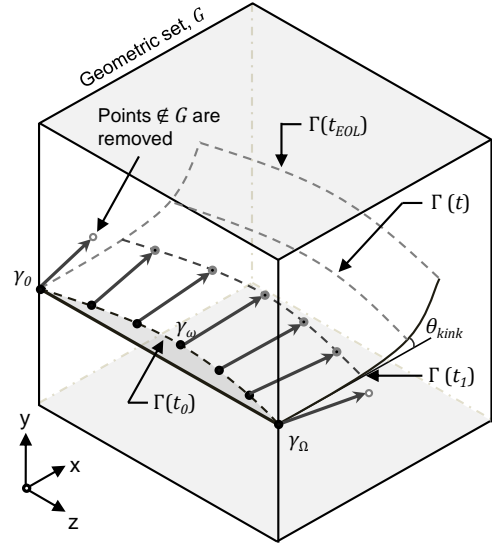


Figure 1. General illustration of the fatigue crack growth model geometrical framework.

eled crack front and its corresponding driving force profile are treated as a single data point to be used to train the surrogate models via supervised machine learning. If each simulation provides  $\eta$  unique couples of crack front and corresponding driving force profiles, the collection of all crack fronts from all training simulations make up a training dataset of size  $\sum_{s=1}^{\Phi} \eta_s$ . For example, 30 crack growth simulations where  $\eta_s = 100$  for  $s = 1, \dots, 30$  yields 3,000 data points that can be used for training. Specifics regarding the fatigue crack growth model can be found in (Leser et al., 2016).

#### 2.4. Prognostic Metrics

It is critical when dealing with prognostics to be able to evaluate the performance of the proposed approach. To this end, prognostic metrics developed by (Saxena, Celaya, Saha, Saha, & Goebel, 2010) were used herein to evaluate the performance of the proposed approach. The hierarchical metrics allow for evaluation of the performance over time, which is desirable because as more information is obtained, better predictions can be made. It should be noted that, since the current work involves fatigue crack growth, all times are measured in cycles. In the case of damage prognosis, RUL is typically of interest and is defined as

$$RUL = t_{EOL} - t_D, \quad (4)$$

where  $t_{EOL}$  is the end of life (EOL) or time of failure, and  $t_D$  is the time at which the last diagnostic measurement was taken. Saxena et al. refer to this as a moving horizon, where

RUL is not only a function of the EOL, but also of the current time. Since they are independent, the balance between the rate at which predictions improve and the time rate of change is critical. If the predictions do not improve quickly enough, they may never prove useful. The problem is exacerbated by the fact that the prognosis procedure cannot be conducted in real time (i.e., there is a finite amount of time after the last measurement before a prediction is made). In this paper, this finite time will be assumed negligible, since the speed of the prognosis was not a primary focus. Mathematically,

$$t_{\text{pred}_\rho} = t_{D_\rho} \text{ for } \rho = 1, \dots, P \quad (5)$$

where  $P$  is the total number of predictions made during the component or structure's lifespan,  $t_{\text{pred}_\rho}$  is the time at which the  $\rho^{\text{th}}$  prediction was made, and, as before,  $t_{D_\rho}$  is the time that the diagnosis data for  $t_{\text{pred}_\rho}$  were gathered. Henceforth, only  $t_D$  will be used for simplicity.

The prognostic metrics applied in this work are as follows:

1. RUL vs. time plot: the basis for all of the prognostic metrics, it is a plot of the RUL predictions and uncertainty over the life of the monitored component or structure.
2. Prognostic horizon,  $PH$ : a measure of time at which the prediction reaches a desired level of accuracy with respect to the EOL.
3.  $\alpha$ - $\lambda$  performance: a measure of how accurate the prediction is with respect to the RUL at a given time. Note that  $\alpha$  and  $\lambda$  are parameters which are used to define the metric and are defined in the subsequent paragraphs.

The RUL vs. time plot is based around the true RUL which is plotted as a straight line, about which RUL predictions and error bounds are drawn for qualitative assessment of the prognostic algorithm's performance as  $t \rightarrow t_{\text{EOL}}$ . The RUL predictions are represented by box plots. Here, the predicted mean and median are represented by a small square symbol and a line dividing the box, respectively. The upper and lower quartiles of the data are represented by the extent of the box, and the whiskers, represented as capped dotted lines, denote the range of the data.

The prognostic horizon and the  $\alpha$ - $\lambda$  performance metrics are more quantitative than the plot alone and depend on three terms:  $\alpha$ ,  $\beta$  and  $\lambda$ . The first is a percent error where  $\alpha \in [0, 1]$  and is used to define a set of upper and lower error bounds,  $\alpha^+$  and  $\alpha^-$ , respectively. Since the two metrics considered here deal with accuracy about two separate quantities, the EOL and RUL, the definition of these bounds differ for each. The same value of  $\alpha$  can and should be used for both metrics.

The  $\beta$  parameter is used to define a portion of probability and is used as a threshold. This value should be set equal to the percentage of the probability in the predicted RUL PDF that the user desires to lie within the  $\alpha$ -bounds, where  $\beta \in [0, 1]$ . In this way,  $\beta$  is dependent on the purpose or mission of the component or structure being monitored. Finally,  $\lambda \in [0, 1]$  and is a time window modifier that simply normalizes the region of the time axis between the time the first prediction is made,  $t_{D_1}$ , and  $t_{\text{EOL}}$ , such that

$$t_{\lambda_\rho} = t_{D_1} + \lambda(t_{\text{EOL}} - t_{D_1}). \quad (6)$$

The  $\alpha$ -bounds for the prognostic horizon metric are defined as

$$\alpha^\pm = RUL \pm \alpha \cdot t_{\text{EOL}}, \quad (7)$$

where  $RUL$  is the true value of RUL calculated using the true EOL,  $t_{\text{EOL}}$ , and Equation 4. The actual metric is defined as

$$PH = t_{\text{EOL}} - t_D^*, \quad (8)$$

where  $t_D^*$  is the first time,  $t_{D_\rho}$ , for which the percentage of probability of the predicted PDF (obtained via integration or a probability mass approximation) within the  $\alpha$ -bounds is greater than or equal to  $\beta$ . Hence, the  $PH$  metric is a measure of time indicating how long it took to reach an acceptable accuracy in the EOL forecast.

Contrary to the prognostic horizon, the  $\alpha$ - $\lambda$  metric quantifies the accuracy of the prediction of the time-varying RUL, and, therefore, the  $\alpha$ -bounded region for this metric decreases as  $t \rightarrow t_{\text{EOL}}$ . These bounds are defined by

$$\alpha^\pm = RUL \cdot (1 \pm \alpha). \quad (9)$$

The metric takes the form of the Boolean expression

$$\alpha\text{-}\lambda \text{ accuracy} = \begin{cases} 1 & \text{if } \pi(RUL_{\text{pred}})_{\alpha^-}^{\alpha^+} \geq \beta \\ 0 & \text{otherwise} \end{cases} \quad (10)$$

where  $\pi(RUL_{\text{pred}})_{\alpha^-}^{\alpha^+}$  is the predicted RUL probability that lies within the  $\alpha$ -bounds. This metric is computed at each  $t_{\lambda_\rho}$ . In the present work, these time values always correspond to  $t_{D_\rho}$  for  $\rho = 1, \dots, P$ . The only difference between these time axes is simply that one is normalized over the region in

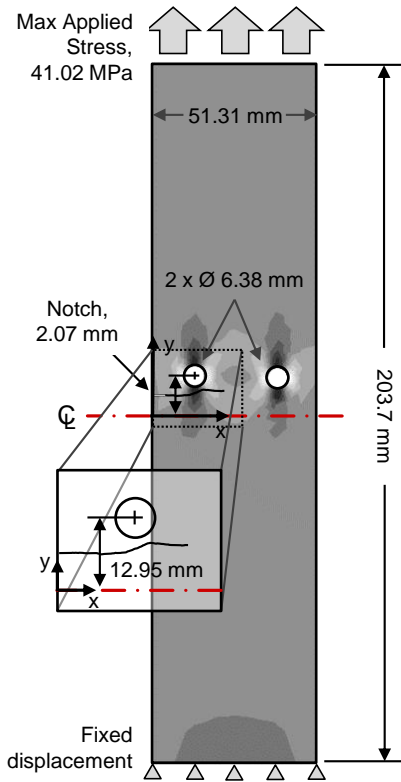


Figure 2. Diagram of the two-hole specimen. Darker shades correspond to higher Von-Mises stresses.

which predictions are made and the other is based on the true time.

### 3. METHODS

#### 3.1. Experimental Setup

To achieve controllable non-planar crack growth, an experiment was developed based on the work in (Ingraffea, Grigoriu, & Swenson, 1991). Two holes were drilled in an edge-notched specimen as shown in Figure 2. When loaded in tension, mixed-mode driving forces were induced by the presence of the holes, causing any cracks growing through their region of influence to kink and grow toward the closest hole. Depending on the  $y$ -coordinate of the notch, herein referred to as  $y_0$ , various degrees of kinking could be achieved. At higher  $y_0$  values, the crack would grow into the hole. At low  $y_0$  values, the crack would grow with minimal kinking. In between these two extremes the crack would slope up toward the hole, peak, and then partially slope back down to a relatively horizontal growth condition before crossing an instability threshold and ultimately failing.

A random notch location between the aforementioned extremes was chosen for the current experiment at  $y_0 = 6.73$  mm, and the edge notch was cut at that location to a length of 2.16 mm using electrical discharge machining (EDM). The crack was grown from the notch under a constant amplitude fatigue stress of 41.0 MPa with a load ratio,  $R = 0.1$ , and a frequency of 10 Hz. Crack tip location was measured at fixed cycle intervals using a traveling optical microscope. The observed crack path from the experiment is plotted in Figure 2. The crack grew into the influence of the hole, exhibited non-planar growth, and then grew to failure. The crack shown is the final configuration before failure was deemed to have occurred. Note that, while through-the-thickness measurements were not available, the crack growth was modeled in three dimensions to demonstrate the capabilities of the model.

The goal of the present work was to utilize damage diagnosis data to accurately predict, with quantified uncertainty, the RUL of a specimen containing an evolving non-planar crack. Predictions were to be made at multiple times during the specimen lifespan to demonstrate the effect of data on the prognosis. For the purpose of this experiment, the damage diagnosis data took the form of crack tip locations in the  $x$ - $y$  plane over time. Since the intention of the presented prognosis framework was to utilize noisy data from in-situ SHM or automated NDE diagnosis systems, the high-precision visual measurements were augmented with Gaussian white noise,  $\epsilon \sim N(0, \sigma^2)$ , in an attempt to replicate results typical of these systems. The SNR was defined here as the reciprocal of the coefficient of variation (Parzen, 1961) for both the  $x$  and  $y$  one dimensional data arrays, such that

$$\text{SNR}_x = \frac{\mu_x}{\sigma_x}, \quad \text{SNR}_y = \frac{\mu_y}{\sigma_y}. \quad (11)$$

Here,  $\mu$  and  $\sigma$  are the mean and standard deviation of the measurements, respectively.

Assuming that an in-situ SHM system would likely be less accurate than an NDE scan, a mounted piezoelectric sensor array was chosen as inspiration for the noise model. A simple linear array would likely have to be mounted somewhere toward the bottom of the specimen and oriented in the  $x$ -direction. Therefore, it was also assumed that  $\text{SNR}_x > \text{SNR}_y$  since the incident waves would be approximately perpendicular to the crack faces growing in the  $x$ -direction. Based on these assumptions,  $\text{SNR}_x = 5$  and  $\text{SNR}_y = 2.5$  for the experiment. The resulting dataset was thinned by 20% and divided into five intervals; i.e., five predictions of RUL would be made, each after a new interval of data was appended to the total set. The vector of times at which these data were gath-

ered  $t_D = [350, 500, 650, 800, 950]^T \times 10^3$  cycles<sup>1</sup>. Figure 3 shows the data divided into intervals overlain on the visually observed crack, near the left hole.

### 3.2. Surrogate Training

The surrogate models responsible for returning crack driving forces were trained using the high-fidelity FE-based fracture software FRANC3D<sup>2</sup> in conjunction with the FE software Abaqus.<sup>3</sup> Training simulations were generated by varying the following two parameters: (i) the initial starting position,  $y_0$ , which is the only parameter directly affecting crack path with respect to the hole, and (ii) the initial crack length  $a_0$ , which is required for initiation from a straight notch of an unknown length.

The training data were developed in three steps. Originally, the number of complete simulations  $\Phi = 30$  as shown in Figure 4. All of the simulations were fixed at a single  $a_0$  and varied  $y_0$  only. Next, 330 additional, single-step simulations with 11 different values for  $a_0$  per each of the original  $y_0$  values were added to the dataset under the assumption that these small cracks would result in paths nearly identical to the original 30 simulations. Finally, the dataset was augmented by manually varying the crack front shape at each growth step, in all simulations. Five different crack front shapes were used ranging from perfectly straight (i.e., a midpoint extension of zero for a parabolic curve) to an exaggerated curve (i.e., a midpoint extension of 0.127 mm). These augmented shapes allowed the surrogates to reach equilibrium during growth in spite of small numerical errors in the crack propagation. In total, the training simulations resulted in 16, 229 training points, each consisting of one unique crack front and its corresponding SIF profiles (i.e.,  $K_I$ ,  $K_{II}$ , and  $K_{III}$  at each front point,  $\gamma_\omega$ ). The crack growth algorithm and surrogate model were verified and validated using FRANC3D simulations that were not part of the original training set along with experimental crack growth data. The details of the training process, the verification, and the validation were reported in (Leser et al., 2016) and will be omitted here for brevity. Replacing the FE-based crack growth simulations with the surrogate-assisted approach yielded a reduction in computation times of three orders of magnitude on average (i.e., from nearly 3 hours per simulation to  $< 7$  seconds).

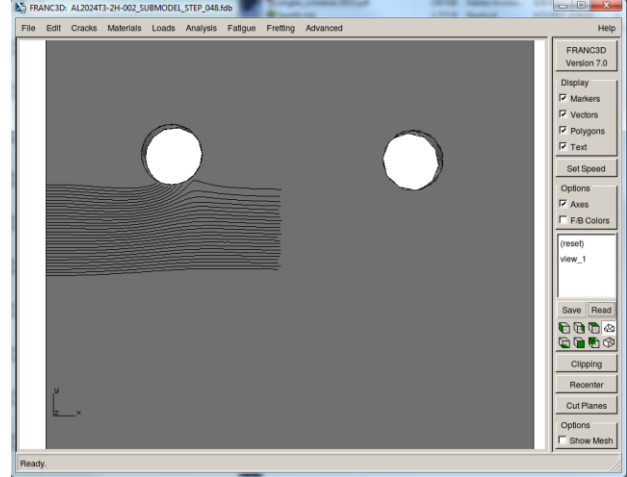


Figure 4. Depiction of the original 30 crack growth simulations comprising the base of the training dataset. Screenshot taken from the fracture analysis software FRANC3D.<sup>1</sup>

### 3.3. Detailing the Crack Growth Model

The conceptual framework of the crack growth model was presented earlier in Section 2.3. Due to its flexibility, a variety of fracture mechanics models can be plugged into this framework. The specific equations used to dictate the fracture growth in the present work are outlined in this section. For more details, the reader is referred to the work in (Leser et al., 2016), which used the same crack growth model.

To incorporate the effects of the load ratio,  $R$ , on the crack growth rate,  $\frac{da}{dN}$ , Walker's modification of the Paris' Law (Walker, 1970),

$$\frac{da}{dN} = C \left[ \frac{\Delta K}{(1-R)^{1-m}} \right]^n, \quad (12)$$

was chosen as the crack growth rate model. Here,  $C$ ,  $m$  and  $n$  are empirical constants and

$$\Delta K = K_{I,max} - K_{I,min}. \quad (13)$$

where  $K_I$  is the mode I SIF. Note that  $R = \frac{K_{I,min}}{K_{I,max}}$ . The mode II SIF,  $K_{II}$  plays a significant role in the kinking behavior of the crack. In the present work, the maximum tangential stress criterion (Erdogan & Sih, 1963) is used to dictate how the crack turns under mixed-mode SIFs,

$$\theta_{kink} = \arg \max_{\theta} \left( K_I^r(\theta) \right), \quad (14)$$

where, ignoring high-order stress terms,

<sup>1</sup>Note that this time vector and all subsequent times herein will be reported as a count of complete fatigue cycles. True time can be obtained by dividing the number of cycles by 10 Hz, or the frequency used for the experiment.

<sup>2</sup>See reference ("FRANC3D Reference Manual, Version 6", 2011)

<sup>3</sup>See reference ("Abaqus/CAE User's Manual, Version 6.12", 2012)

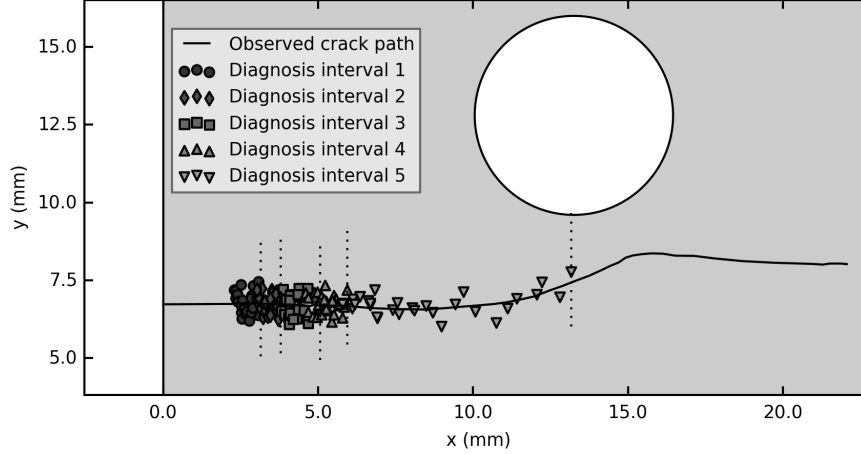


Figure 3. Damage diagnosis obtained via visual measurements of the crack tip location with added noise and ( $\text{SNR}_x = 5$  and  $\text{SNR}_y = 2.5$ ). The dotted lines represent the boundaries of the diagnosis intervals and represent the five points in time at which predictions were made;  $t_D = [350, 500, 650, 800, 950]^T \times 10^3$  cycles, respectively.

$$\begin{aligned} K_I^r(\theta) &= \sigma_{\theta\theta} \sqrt{2\pi r} \\ &= \cos \frac{\theta}{2} \left[ K_I \cos^2 \frac{\theta}{2} - \frac{3}{2} K_{II} \sin(\theta) \right]. \end{aligned} \quad (15)$$

is the resolved mode I SIF and  $\sigma_{\theta\theta}$  is the tangential stress. Combining Equations 13 and 15, an effective equivalent  $\Delta K$  can be defined as

$$\Delta K_{ee} = K_{I,max}^r - K_{I,min}^r. \quad (16)$$

which can then be applied to Equation 12.

In the three-dimensional implementation of the crack growth model, these equations are applied to each crack front point,  $\gamma_\omega$ , to determine the crack growth rate,  $\frac{da}{dN_\omega}$ . The crack front is then advanced using a median extension approach, where the median extension is defined as

$$\Delta a_\omega = \Delta a_{median} \left[ \frac{\frac{da}{dN_\omega}}{\frac{da}{dN_{median}}} \right], \quad (17)$$

and  $\Delta a_{median}$  is a user-defined value, and  $\frac{da}{dN_{median}}$  is the median of  $\frac{da}{dN_\omega}$  for  $\omega = 1, \dots, \Omega$ . Using the median extension approach requires that the number of cycles to grow the front at each point be computed through integration of the crack growth rate equation over  $\Delta a_\omega$ ,

$$\Delta N_\omega = \int_0^{\Delta a_\omega} C^{-1} \left[ \frac{\Delta K_{ee}}{(1-R)^{1-m}} \right]^{-n} d(\Delta a_\omega). \quad (18)$$

This means that the number of cycles returned at each front point will be different, albeit often with a standard deviation,  $\sigma_{N_\omega} < 1$  cycle. The final cycle count used for the crack growth step,  $\Delta N^* = \sum_{\omega=1}^{\Omega} \Delta N_\omega$ . It should also be noted that the SIF term is a continuous function of the crack length, so an assumption must be made as to its functional form. This relationship was assumed to be linear in the current work.

Finally, failure was dictated by a critical mode I SIF criterion. If, at any crack front point,  $K_{I,max} > K_{IC}$ , where  $K_{IC}$  is the critical mode I SIF and is a material property, then failure is deemed to have occurred. Uncertainty in  $K_{IC}$  was not considered. Instead, the experimentally observed crack geometry was inserted into a FE model of the specimen using FRANC3D, and the value of  $K_{I,max}$  at failure was calculated and used to set  $K_{IC} = 834 \text{ MPa}\sqrt{\text{mm}}$ .

## 4. RESULTS

### 4.1. Sensitivity Analysis

Global sensitivity analysis was conducted using Saltelli's algorithm (Saltelli et al., 2008). The parameters considered in the sensitivity analysis were the initial  $y$ -coordinate of the crack,  $y_0$ , the initial crack length,  $a_0$ , and the Walker model parameters,  $C, n, R$ , and  $m$ . The initial distributions were chosen to encompass the extremes of the knowledge of the specimen and previous research of the crack growth rates in aluminum alloy 2024-T3. While the RUL is the primary output of interest for prognosis, the cycle values at EOL over the parameter space varied over multiple orders of magnitude, causing difficulties when calculating the sensitivity indices. Instead, an approach was adopted in which the variance of crack tip coordinates in the  $x$  and  $y$  directions due to the



varying parameters were used to calculate the first-order and total-effect Sobol' indices over time.

The sensitivity analysis results for the  $x$ -coordinate are shown in Figure 5. The figure shows Sobol' indices plotted over a normalized time for simplicity (i.e., cycles divided by true end of life). Examining the first-order indices,  $S_i$ , the Paris coefficient,  $C$ , and the Paris exponent,  $n$ , are the most influential parameters, which is to be expected as these are the two primary drivers of the crack growth rate. The effect of the load ratio,  $R$ , was also evident, and its Sobol' indices overtook  $n$  as the number of cycles approaches the end of life. The remaining parameters,  $a_0$  and  $y_0$ , are approximately zero over time. While not clear in the figures, both the first-order and total-effect indices for  $a_0$  exhibit peaks at time zero, which is intuitive since it was the only parameter affecting the value of  $x$  for that instant. This peak was ignored since these values quickly decline for times greater than zero. By definition, the total-effect indices must equal zero for a parameter to be considered non-influential, which is approximately the case for both  $a_0$  and  $y_0$ . All of the crack growth rate parameters showed an appreciable total-effect index and, therefore, were considered influential with respect to the crack growth in the  $x$ -direction. Sensitivity indices for the crack tip  $y$ -coordinate over time were also obtained, and, as expected, only  $y_0$  had an appreciable first-order effect, with the remainder of model parameters at or near zero.

Based on all of the information obtained from the global sensitivity analysis, only  $a_0$  could be fixed with reasonable confidence that it was non-influential. The remainder of the parameters were considered in the Bayesian inference problem. Regardless, valuable information about the effect and interaction of parameters in the context of the crack growth model was gained. A global sensitivity analysis, besides the obvious utility, also tests the robustness of the model as it requires evaluations over the entire parameter space.

## 4.2. Prognosis

### 4.2.1. Parameter estimation & uncertainty quantification

A solution to the Bayesian inverse problem of Equation 2 was obtained using the experimentally observed crack tip measurements in conjunction with Markov chain Monte Carlo (MCMC) sampling. Parameter estimation using MCMC was conducted five times in total using the data in Figure 3, once for each interval as marked. Specifically, the uncertainty in parameters was estimated at 350, 500, 650, 800, and 950 thousand fatigue cycles into the experiment, respectively. The data at each interval consisted of all of the measurements up to the respective cycle; i.e., the data used at a particular cy-

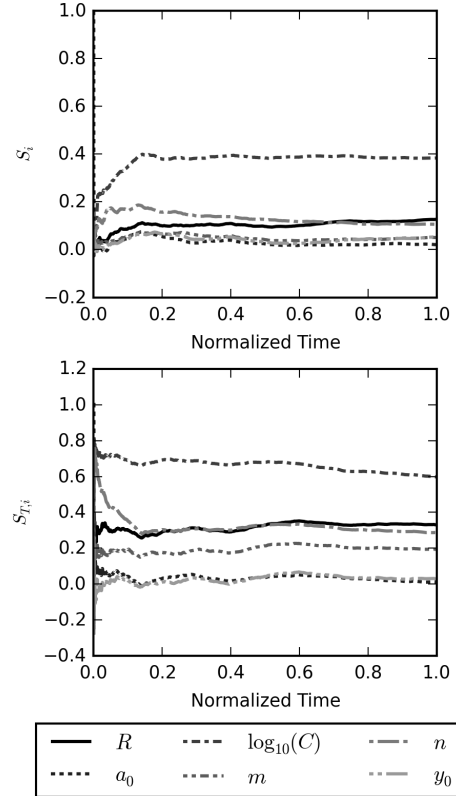


Figure 5. First-order and total-effect Sobol' indices for crack tip  $x$  location over  $1 \times 10^6$  cycles (normalized)

cle included all of the measurements from the beginning of the test up to that point in time. Non-informative, or uniform, prior distributions were used for all of the parameters at each interval as shown in Table 1. This implies that each MCMC run was considered independent from the others, and no prior information was passed between the subsequent runs as might be the case for a true Bayesian updating scheme. The adaptive Metropolis algorithm included in the PyMC python package (Patil, Huard, & Fonnesbeck, 2010) was used to generate  $2 \times 10^5$  samples, with a conservative burn-in of  $1 \times 10^5$  samples to ensure Markov chain stabilization. Geweke's time-series approach was utilized to diagnose chain convergence (Geweke, 1992).

Parameter estimation results in the form of marginal probability distribution functions (PDF) for all parameters and for all five data intervals are shown in Figure 6. The bounds used during parameter estimation for  $R$  and  $m$  were significantly tighter than those used during the sensitivity analysis, which was based on a conservative interpretation of the expected accuracy of the load frame used in the experiments. These parameters were unidentifiable given the current set of data, and thus the MCMC procedure returned uniform distributions (i.e., returned the prior distribution). It is possible that this

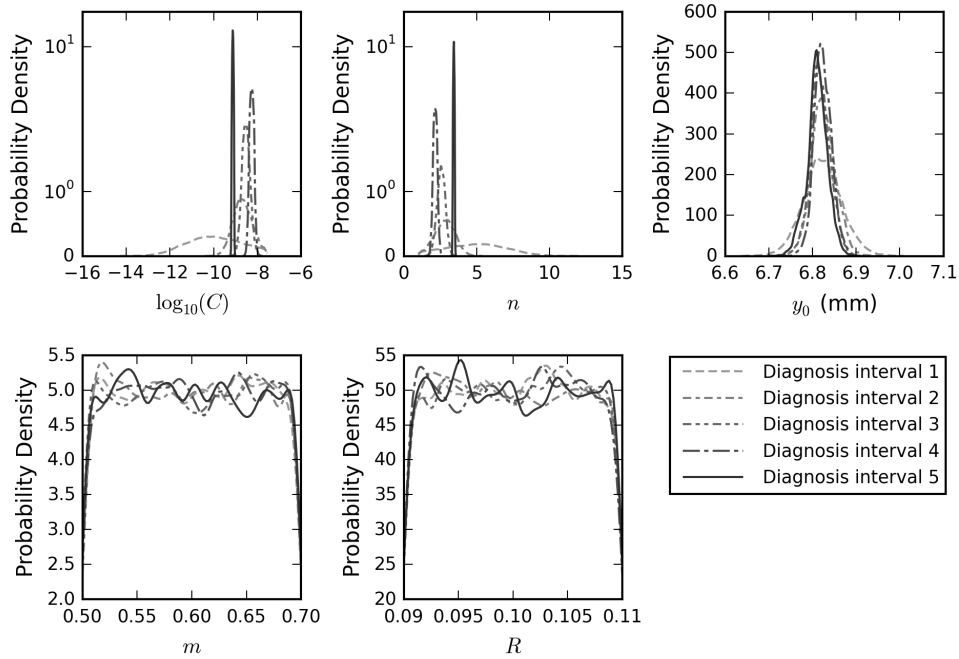


Figure 6. Resulting PDFs from the Bayesian parameter estimation process using MCMC, updated over the 5 diagnosis intervals. These intervals correspond to the values in  $t_D = [350, 500, 650, 800, 950]^T \times 10^3$  cycles, respectively, which represent the times at which the last data point in the interval was collected.

Table 1. Parameter distributions for Markov chain Monte Carlo sampling

Parameter	Distribution	Description
$\log_{10}(C)$	$U(-20, -1)$	$\log_{10}$ of the Paris' Law coefficient
$m$	$U(0.5, 0.7)$	Load ratio exponent
$n$	$U(1.0, 20)$	Paris' Law exponent
$R$	$U(0.09, 0.11)$	Load ratio
$y_0$	$U(0.01, 0.365)$	Crack initiation $y$ -coordinate

was due to the tight bounds enforced through prior knowledge. Examining the remaining parameters in the figure, the uncertainty decreases as more data are added. However, it is also important to notice that the distributions exhibit a significant shift at time  $t_{D_s}$  after the last interval, a topic that will be discussed more in the subsequent sections.

Figure 7 shows the pairwise plots of the sampled parameters after the fourth data interval was obtained. The samples indicate a strong correlation between the Paris' Law parameters,  $C$  and  $n$ . This correlation is commonly reported in fracture mechanics literature (Cortie, 1991; Carpinteri & Paggi, 2007). This correlation indicates that these two parameters are not mutually identifiable. The correlation also violates the assumptions of Saltelli's global sensitivity analysis algorithm, which was used herein and assumes independent parameters. Future work should investigate other methods such

as those presented in (Xu & Gertner, 2008) or (Li & Mahadevan, 2016) which do not require this assumption. The shift in parameter distributions can be seen again by comparing Figure 7 with the pairwise plots from the fifth update shown in Figure 8.

#### 4.2.2. Uncertainty propagation and RUL prediction

Once the uncertainty in the model parameters was quantified, the prognosis could be formed by propagating these uncertainties through the crack growth model and extrapolating forward in time to the failure condition  $K_{I,max} > K_{IC}$ . This process was conducted using a Monte Carlo sampling approach in which 25,000 samples were drawn from the parameter distributions and passed to the model, which then simulated crack propagation up to the EOL condition. The final cycle counts for all 25,000 simulations were aggregated to form an EOL distribution. Using Equation 4, the EOL distribution can easily be converted to an RUL distribution. This procedure was repeated five times, once for each interval, and all simulations were conducted in parallel utilizing high performance computing.

The resulting RUL distributions are presented in the form of an RUL vs. time plot in Figure 9. The shaded strip and cone regions represent the  $\alpha = 0.1$  accuracy intervals associated

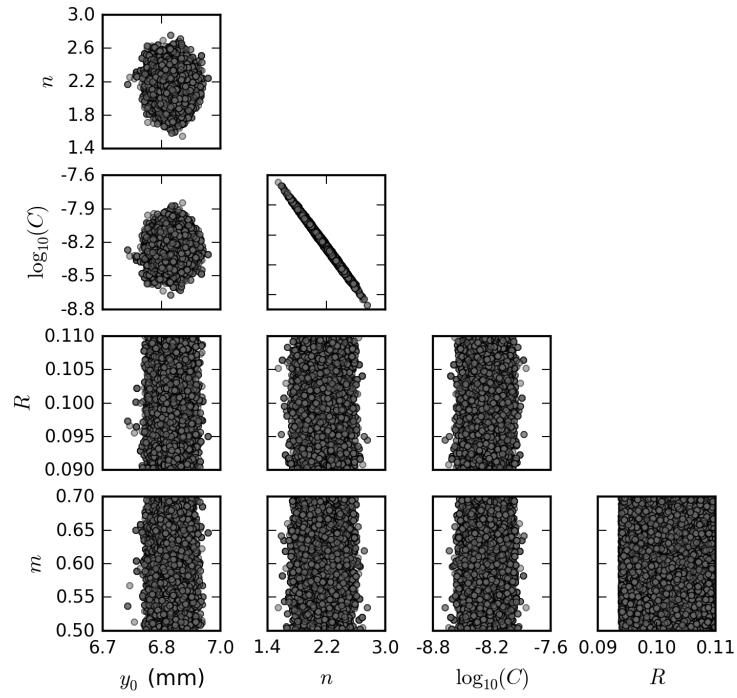


Figure 7. Joint samples obtained from the parameter estimation for the 4<sup>th</sup> diagnosis interval, or  $t_{D_4} = 800 \times 10^3$  cycles.

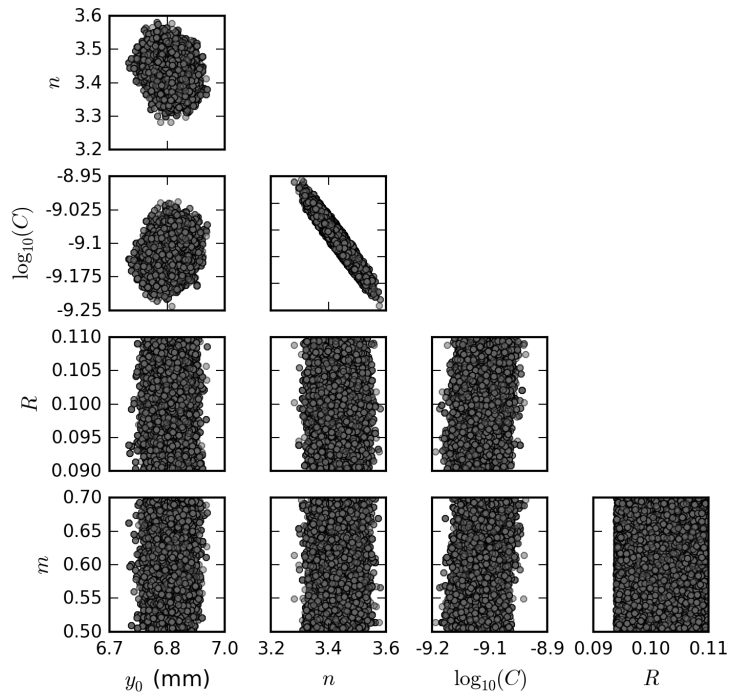


Figure 8. Joint samples obtained from the parameter estimation for the 5<sup>th</sup> diagnosis interval, or  $t_{D_5} = 950 \times 10^3$  cycles.

with the  $PH$  and  $\alpha$ - $\lambda$  prognostic metrics, respectively. As discussed previously, the constant-width strip region can be interpreted as an accuracy measure of how well the EOL was predicted, while the cone indicates how well the RUL was predicted. The cone shape is an artifact of the true RUL being a monotonically decreasing function of time. Similar to the parameter estimation results, the first four RUL predictions exhibit convergence with a steady decrease in associated uncertainty. However, it can now be observed that these predictions actually diverge from the true solution. Again, after the last diagnosis interval at  $t_{D_5}$ , the PDF shifts.

While it was difficult to determine whether the shift shown in the parameter PDFs resulted in better accuracy, the shift in the RUL distribution can be quantified since the ground truth value is known. As shown, the final prediction enters both  $\alpha$  bounded regions. Figure 10 shows the predicted PDF of the RUL at this point (i.e., obtained after the fifth data interval) for clarity. The double dotted lines represent the  $\alpha$ -bounds associated with the  $\alpha$ - $\lambda$  metric. The difference between the mean prediction and the true RUL is 4,625 cycles, or a percent error of 5.9%. While this result may seem satisfactory, the ability to accurately predict the RUL is only part of a successful damage prognosis scheme.

An accurate prediction must be made early enough for the proper action to be taken, which is the motivation of the prognosis metrics presented in (Saxena et al., 2010) discussed earlier. Setting  $\alpha = 0.1$  and  $\beta = 0.25$ , the prognostic horizon,  $PH = 78,537$  cycles. This represents the earliest time that at least 25% of the probability in the forecasted RUL distribution lies within the  $\alpha$ -bounds. Here,  $PH$  corresponds to the prediction made after the fifth data interval was gathered (see Figure 9). Even setting  $\beta = 0.1$ , the prognostic horizon,  $PH = 528,537$  cycles. This corresponds to the second data interval. However, as shown in Figure 9, the following data update results in a RUL distribution that has near zero probability within the  $\alpha$ -bounds.

Proceeding further through the prognostic metric hierarchy, the  $\alpha$ - $\lambda$  metrics for the five data intervals are shown in Table 2. This metric clearly captures the poor performance for the first four data intervals, and quantifies the percentage of time between the first prediction and the EOL. This metric utilizes the cone-shaped bounds, which, in general, provide a better prognostic evaluation since the RUL is the true quantity of interest. Only 22% of the time available for predictions remains when the predicted RUL distribution satisfies the  $\alpha$ - $\lambda$  metric. The  $\alpha$ - $\lambda$  test can also be visualized as demonstrated in Figure 11. As opposed to presenting a Boolean pass or fail, this figure shows the probability of the RUL PDF that lies within

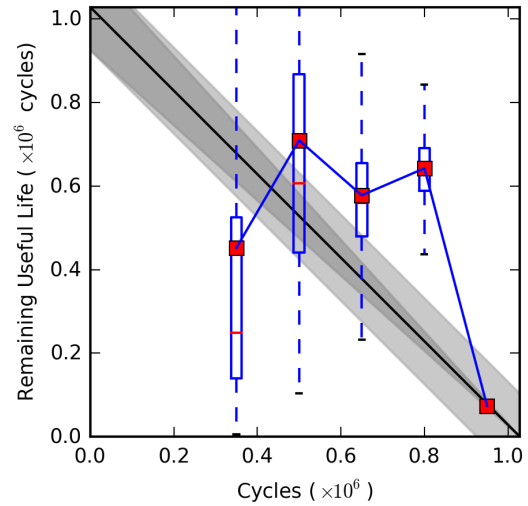


Figure 9. RUL vs. time plot for the five updates of the diagnosis dataset. The solid black line represents the experimentally observed RUL over time. The shaded strip (constant width) and the cone-shaped regions represent the  $\alpha = 0.1$  accuracy bounds corresponding to the  $PH$  and  $\alpha$ - $\lambda$  metrics, respectively. The probabilistic prediction of RUL at each time,  $t_{D_i}$ , is represented by a box plot as described in Section 2.4.

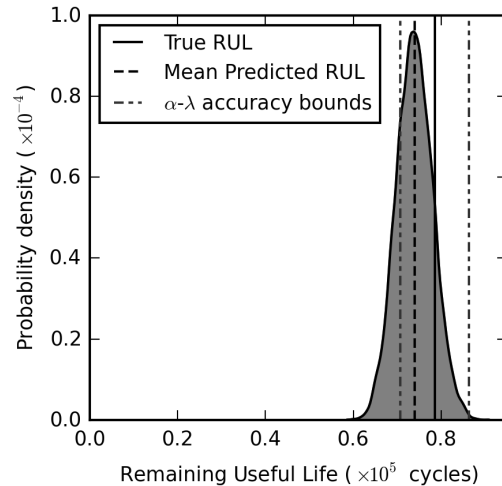


Figure 10. PDF of the final RUL prediction (i.e., obtained using all five intervals of damage diagnosis data).

the cone-shaped  $\alpha$ -bounds, regardless of the value of  $\beta$ . The double  $x$ -axes show the time in cycles and as a percentage of time in the available prediction window. The divergence from the true RUL is clearly shown here between the second and fourth intervals along with the sudden shift in accuracy after the fifth interval. The improvement in accuracy results in 78% of the predicted probability lying within the  $\alpha$ -bounds, but with only 12% of the  $\lambda$ -window remaining.

## 5. DISCUSSION

The divergence of the predictions would be concerning if the presented specimen was instead a real-world structure or safety-critical component operating in the field. The idea that the forecasts could shift from the true value while decreasing in uncertainty is dangerous as it can result in either false-positives or false-negatives, both of which could have significant consequences. The first suspect in the search for a reason behind this divergence is the model. However, the model clearly shows that it is capable of capturing the true RUL given adequate data. The model cannot be entirely ruled out without further testing as there may be a form of model discrepancy present in the region of growth occurring around the fifth data update. Model discrepancy refers to cases where the model is incapable of capturing certain physically observed behavior. A simple analogy would be attempting to fit a higher-order polynomial without enough degrees of freedom. Future work should investigate the existence and effect of potential model discrepancies not only of the proposed surrogate modeling approach, but also of the training simulator FRANC3D. Note that, as shown in (Leser et al., 2016), the proposed model matches almost exactly with FRANC3D-derived validation cases.

The parameters chosen for the analysis represent another way in which the model could be causing poor predictions. The choice to remove the parameter  $a_0$  based on the sensitivity analysis could have unforeseen consequences. Perhaps this parameter was more influential than shown. Furthermore, upon examination of the differences between the joint samples in Figures 7 and 8, there is a change observed in the parameter relationships. In the final update, the sharp, almost linear correlation between  $C$  and  $n$  that is so commonly reported in fracture mechanics literature is much less pronounced. Additionally, slight correlations now can be observed between the Paris' Law parameters and  $y_0$ , as well as between  $C$  and both Walker parameters. This indicates that the interactions within the parameter space enforced by the prior distributions may not be completely understood. It is possible that the Walker parameters require a less restrictive prior, and that the uncertainty in the loading was greater than

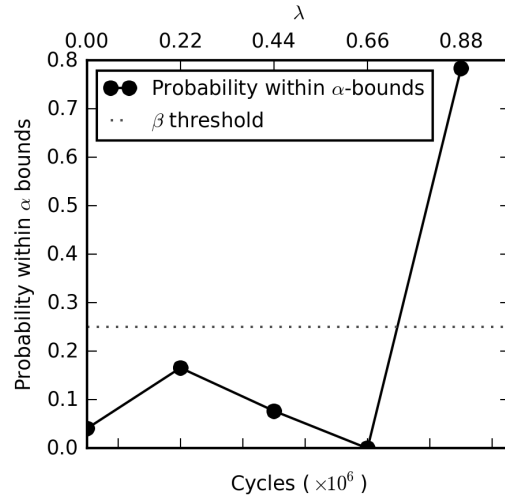


Figure 11. Probability within the  $\alpha$ - $\lambda$  metric  $\alpha$ -bounds (i.e., the cone-shaped bounds). The  $\lambda$  axis represents the percentage of time between the first prediction and the EOL.

Table 2.  $\alpha$ - $\lambda$  test results with  $\alpha = 0.1$  and  $\beta = 0.25$ .

Cycle	$\lambda$	Passes $\alpha$ - $\lambda$ test
350,000	0.00	False
500,000	0.22	False
650,000	0.44	False
800,000	0.66	False
950,000	0.88	True

previously thought. Future work should include a more expansive study of these correlations that appear after the fifth update.

The model may be a part of the issues highlighted herein, but, based on the sudden shift in parameter distributions and the final PDF of the RUL, a stronger argument could be made against the data instead. The crack growth data in the fifth interval are the first of which that capture the primary non-planar features of the crack behavior. It is not a coincidence that this coincides with the shift in the prediction, and it is likely that the shift would be more gradual if given one data point at a time from this interval. This result is intuitive. However, a more important concern is whether or not the data in the second through fourth intervals are somehow negatively impacting the results. This is the region where a divergence from the true RUL is observed. Even if it is accepted that forecasts will only be usable after data have been gathered in the non-planar region, the question remains whether or not the data before that point are valuable or detrimental. It is possible that removing the middle three intervals and only using the first and fifth might reduce the uncertainty in the

final prediction. After all, if accurate predictions can only be made after 800,000 cycles into the fatigue life, it would still be desirable to improve the accuracy within the time that remains. High levels of accuracy in this region are especially important considering how close it is to the EOL.

All of the above issues are driven by the fact that the crack growth is non-planar, which supports the idea that real-world prognosis must be of concern to researchers in the field of damage prognostics. The number of issues in all phases of a prognostic framework appear to increase with complexity in the crack growth behavior. Data become harder to obtain and, therefore, more uncertain, and the modeling is more complicated and increases the likelihood of model discrepancies or user error. Both of these issues then complicate Bayesian inference and uncertainty propagation, culminating in difficulties reaching the final goal: an accurate forecast of future damage growth.

## 6. CONCLUSION

A flexible, high-fidelity yet rapid probabilistic framework for fatigue damage prognosis was demonstrated for a metallic specimen exhibiting non-planar crack growth. Damage diagnosis data in the form of visual crack tip measurements with added noise were used to quantify the uncertainty in crack growth model parameters through Bayesian inference and Markov chain Monte Carlo sampling. The computational burden associated with high-fidelity crack growth models was neutralized through the use of a previously developed modeling approach in which expensive finite element-based computation of crack driving forces was replaced with an efficient surrogate model. Driving forces returned by the surrogate model were fed to a fully three-dimensional fracture mechanics algorithm for crack propagation. The flexibility of the crack growth model was demonstrated through a global sensitivity analysis followed by the parameter estimation procedure. Following their quantification, parameter uncertainties were propagated forward in time to generate a probabilistic prediction of the specimen's remaining useful life.

Results showed an initial divergence from the true solution followed by a sharp increase in accuracy near the specimen end of life. The shift in accuracy corresponded to the acquisition of observations of the primary non-planar features of the crack, suggesting model discrepancy and faults in the data (e.g., lack of data or misleading data) as possible reasons for the early divergence in forecasts. Future work should investigate the role of both factors, as a system whose uncertainty decreases but diverges from the truth is potentially dangerous. Upon inclusion of the data from the primary non-planar

region of crack growth, the new predicted mean converged to the true remaining useful life value with a percent error of only 5.9% and with 78% of the predicted probability lying within 10% of the true value.

The discrepancy between the final prediction and those before it is an important result from this work, as it demonstrates not only the importance of rigorous prognostic verification and validation, but it also offers a glimpse into some of the real-world challenges that need to be addressed in the damage prognosis field. The issues highlighted herein can be directly traced to the non-planar nature of the crack, suggesting that models must be developed to accurately capture this behavior. Continued research in the area of rapid, high-fidelity prognostic methods is paramount if health management tools are to reach their full potential.

## REFERENCES

- Abaqus/CAE User's Manual, Version 6.12 [Computer software manual]. (2012).
- Carpinteri, A., & Paggi, M. (2007). Self-similarity and crack growth instability in the correlation between the paris constants. *Engineering Fracture Mechanics*, 74(7), 1041–1053.
- Chiachio, J., Chiachio, M., Saxena, A., Rus, G., & Goebel, K. (2013). An energy-based prognostics framework to predict fatigue damage evolution in composites. In S. Sankararaman & I. Roychoudhury (Eds.), *Proceedings of the Annual Conference of the Prognostics and Health Management Society* (pp. 363–371). New York: Prognostics and Health Management Society.
- Cortie, M. (1991). The irrepressible relationship between the paris law parameters. *Engineering Fracture Mechanics*, 40(3), 681–682.
- Erdogan, F., & Sih, G. (1963). On the crack extension in plates under plane loading and transverse shear. *Journal of Fluids Engineering*, 85(4), 519–525.
- Farrar, C. R., & Worden, K. (2012). *Structural health monitoring: a machine learning perspective*. John Wiley & Sons.
- FRANC3D Reference Manual, Version 6 [Computer software manual]. (2011).
- Geweke, J. (1992). Evaluating the accuracy of sampling-based approaches to the calculation of posterior moments. In J. Bernardo & J. Berger (Eds.), *Bayesian Statistics 4: Proceedings of the Fourth Valencia International Meeting* (pp. 169–193). Oxford, UK: Oxford University Press.
- Gobbato, M., Conte, J. P., Kosmatka, J. B., & Farrar, C. R. (2012). A reliability-based framework for fatigue damage prognosis of composite aircraft structures. *Probabilistic Engineering Mechanics*, 29, 176 - 188.

- Gope, P. (1999). Determination of sample size for estimation of fatigue life by using Weibull or log-normal distribution. *International Journal of Fatigue*, 21(8), 745–752.
- Hombal, V., Ling, Y., Wolfe, K., & Mahadevan, S. (2012). Two-stage planar approximation of non-planar crack growth. *Engineering Fracture Mechanics*, 96, 147–164.
- Hombal, V., & Mahadevan, S. (2013). Surrogate modeling of 3D crack growth. *International Journal of Fatigue*, 47, 90–99.
- Ingraffea, A., Grigoriu, M., & Swenson, D. (1991). Representation and probability issues in the simulation of multi-site damage. In S. Atluri, S. Sampath, & P. Tong (Eds.), *Structural integrity of aging airplanes* (pp. 183–197). Berlin: Springer-Verlag.
- Johnston, G. (1983). Statistical scatter in fracture toughness and fatigue crack growth rate data. In J. Bloom & J. Ekvall (Eds.), *Probabilistic fracture mechanics and fatigue methods: Applications for structural design and maintenance* (pp. 42–66). Philadelphia: American Society for Testing and Materials.
- Laloy, E., & Vrugt, J. A. (2012). High-dimensional posterior exploration of hydrologic models using multiplicity DREAM (ZS) and high-performance computing. *Water Resources Research*, 48(1), 239–249.
- Leser, P. E., Hochhalter, J. D., Warner, J. E., Newman, J. A., Leser, W. P., Wawrzynek, P. A., & Yuan, F.-G. (2016). IWSHM 2015: Probabilistic fatigue damage prognosis using surrogate models trained via three-dimensional finite element analysis. *Structural Health Monitoring (currently online only)*. doi: 10.1177/1475921716643298.
- Li, C., & Mahadevan, S. (2016). An efficient modularized sample-based method to estimate the first-order Sobol' index. *Reliability Engineering & System Safety*, 153, 110–121.
- Ling, Y., & Mahadevan, S. (2012). Integration of structural health monitoring and fatigue damage prognosis. *Mechanical Systems and Signal Processing*, 28, 89–104.
- Liu, Y., & Mahadevan, S. (2009). Probabilistic fatigue life prediction using an equivalent initial flaw size distribution. *International Journal of Fatigue*, 31(3), 476–487.
- Neiswanger, W., Wang, C., & Xing, E. (2014). Asymptotically exact, embarrassingly parallel MCMC. In N. Zhang & J. Tian (Eds.), *Proceedings of the 30th Conference on Uncertainty in Artificial Intelligence* (pp. 623–632). Oregon: AUAI Press Corvallis.
- Parzen, E. (1961). Mathematical considerations in the estimation of spectra. *Technometrics*, 3(2), 167–190.
- Patil, A., Huard, D., & Fonnesbeck, C. J. (2010). PyMC: Bayesian stochastic modelling in Python. *Journal of Statistical Software*, 35(4), 1–81.
- Peng, T., He, J., Xiang, Y., Liu, Y., Saxena, A., Celaya, J., & Goebel, K. (2015). Probabilistic fatigue damage prognosis of lap joint using Bayesian updating. *Journal of Intelligent Material Systems and Structures*, 26(8), 965–979.
- Peng, T., Liu, Y., Saxena, A., & Goebel, K. (2015). In-situ fatigue life prognosis for composite laminates based on stiffness degradation. *Composite Structures*, 132, 155–165.
- Saltelli, A., Ratto, M., Andres, T., Campolongo, F., Cariboni, J., Gatelli, D., ... Tarantola, S. (2008). *Global sensitivity analysis: the primer*. Chichester, West Sussex, UK: John Wiley & Sons.
- Sankararaman, S., Ling, Y., & Mahadevan, S. (2011). Uncertainty quantification and model validation of fatigue crack growth prediction. *Engineering Fracture Mechanics*, 78(7), 1487–1504.
- Sankararaman, S., Ling, Y., Shantz, C., & Mahadevan, S. (2011). Uncertainty quantification in fatigue crack growth prognosis. *International Journal of Prognostics and Health Management*, 2(1), 1–15.
- Saxena, A., Celaya, J., Saha, B., Saha, S., & Goebel, K. (2010). Metrics for offline evaluation of prognostic performance. *International Journal of Prognostics and Health Management*, 1(1), 4–23.
- Smith, R. C. (2013). *Uncertainty quantification: Theory, implementation, and applications*. Philadelphia: SIAM.
- Ter Braak, C. J. (2006). A Markov chain Monte Carlo version of the genetic algorithm Differential Evolution: easy Bayesian computing for real parameter spaces. *Statistics and Computing*, 16(3), 239–249.
- Van Rossum, G., & Drake, F. J. (2011). *An introduction to Python*. Godalming, Surrey, UK: Network Theory Ltd.
- Vrugt, J. A., Ter Braak, C., Diks, C., Robinson, B. A., Hyman, J. M., & Higdon, D. (2009). Accelerating Markov chain Monte Carlo simulation by differential evolution with self-adaptive randomized subspace sampling. *International Journal of Nonlinear Sciences and Numerical Simulation*, 10(3), 273–290.
- Walker, K. (1970). The effect of stress ratio during crack propagation and fatigue for 2024-T3 and 7075-T6 aluminum. In M. Rosenfield (Ed.), *Effects of environment and complex load history on fatigue life* (pp. 1–14). Philadelphia: American Society for Testing and Materials.
- Xu, C., & Gertner, G. Z. (2008). Uncertainty and sensitivity analysis for models with correlated parameters. *Reliability Engineering & System Safety*, 93(10), 1563–1573.